INTERNATIONAL JOURNAL FOR NUMERICAL METHODS IN FLUIDS
Int. J. Numer. Meth. Fluids 2002; **39**:657–673 (DOI: 10.1002/fld.356)

Anisotropic mesh adaptation: towards user-independent, mesh-independent and solver-independent CFD. Part II. Structured grids

Djaffar Ait-Ali-Yahia[1], Guido Baruzzi[2], Wagdi G. Habashi[1,2,3,*,†], Michel Fortin[4], Julien Dompierre[5] and Marie-Gabrielle Vallet[5]

[1]*Pratt & Whitney Canada, 1000 Marie-Victorin (01SR4), Longueuil, Que., Canada J4G 1A1*
[2]*Newmerical Technologies, Inc., 680 Sherbrooke West, Montreal, Que., Canada H3A 2M7*
[3]*CFD Lab, Department of Mechanical Engineering, McGill University, 688 Sherbrooke West, Montreal, Que., Canada H3A 2S6*
[4]*Département de Mathématiques et Statistique, Université Laval, Ste-Foy, Que., Canada, G1K 7P4*
[5]*Centre de Recherche en Calcul Appliqué, 5160, boul. Décarie, Montreal, Que., Canada H3X 2H9*

SUMMARY

The present paper is the second article in a three-part series on anisotropic mesh adaptation and its application to (2-D) structured and unstructured meshes. In the first article, the theory was presented, the methodology detailed and brief examples given of the application of the method to both types of grids. The second part details the application of the mesh adaptation method to structured grids. The adaptation operations are restricted to mesh movement in order to avoid the creation of hanging nodes. Being based on a spring analogy with no restrictive orthogonality constraint, a wide grid motion is allowed. The adaptation process is first validated on analytical test cases and its high efficiency is shown on relevant transonic and supersonic benchmarks. These latter test cases are also solved on adapted unstructured grids to provide a reference for comparison studies. The third part of the series will demonstrate the capability of the methodology on 2-D unstructured test cases. Copyright © 2002 John Wiley & Sons, Ltd.

KEY WORDS: finite element method; error estimation; structured grids; unstructured grids; triangular element; grid adaptation; spring analogy; mesh movement

1. INTRODUCTION

Unstructured meshes based on triangular elements have had a large success in efficiently resolving complex two-dimensional (2-D) flow problems. Combined with hexahedral/prismatic elements, they will almost certainly dominate the next generation of 3-D CFD codes due to

* Correspondence to: W. G. Habashi, CFD Lab, Department of Mechanical Engineering, McGill University, 688 Sherbrooke Street West, 7th Floor, Montreal, Que., Canada H3A 2S6.
† E-mail: wagdi.habashi@mcgill.ca

Received 6 March 2001
Revised 24 January 2002

Copyright © 2002 John Wiley & Sons, Ltd.

their ability to mesh complex geometries in a systematic way and providing a natural setting for adaptation [1, 2] with no major changes to a flow solver.

In the meantime, structured meshes remain dominant in cutting-edge CFD of 2- and 3-D industrial applications. Structured-grid codes are robust, at an advanced stage of maturity and converge complex flow problems for a wide range of flow conditions. This, in no small measure, is helped by their ability to include multigrid acceleration techniques in a more straightforward manner than unstructured solvers.

This second paper presents an enhancement to structured solvers for efficiently resolving unidirectional flow phenomena, such as shocks and boundary layers. A grid adaptation method is described and a thorough evaluation of its performance is presented for 2-D structured grids. Although additional adaptation operations, such as *h*- or *p*-methods [3] could be applied to structured grids, the present approach is limited to mesh movement to remain portable by avoiding hanging nodes which would require special treatment within a flow solver. The current *r*-strategy is based on a spring analogy that has no restrictive orthogonality constraint, hence allowing wider grid motion.

The mesh movement strategy is first validated on structured triangular and quadrilateral grids for a non-CFD test case (exact solution). These cases vividly demonstrate that, when a prescribed uniform metric is imposed, it will result in a completely uniform mesh in the Euclidean sense, no matter what the starting grid was. Having proven mesh adaptation in reverse, the AGARD01–05 benchmarks [4] are then used to investigate the coupling of the moving-node scheme with a flow solver. These test cases consist of inviscid, transonic and supersonic flows over a NACA 0012 airfoil and demonstrate the innate ability of the proposed scheme in efficiently, but most importantly cost effectively, resolving most shock situations, always starting from the same initial structured grid.

2. EDGE-BASED ERROR ESTIMATOR

The theory behind the mesh adaptation technique has been expounded in Part I [5] of this paper series. However, to make this second part somewhat self-contained, a brief review of the error estimator is given.

The error estimator is based on interpolation error theory. For FEM/FVM with linear basis functions, the error is dominated by the quadratic truncation terms and is hence proportional to the Hessian matrix $\boldsymbol{H}$. The components of $\boldsymbol{H}$ are given by the second derivatives of the numerical solution. Since the solution is only piecewise linear, a weak formulation combined with mass lumping has to be used to recover an approximate second derivative. The Hessian $\boldsymbol{H}$ is further modified to define a symmetric positive-definite Hessian, $\boldsymbol{M}$, by taking the absolute values of its eigenvalues.

Using differential geometry, the length $e(\gamma)$ of an edge γ in the metric $\boldsymbol{M}$ is defined by

$$e(\gamma) = \int_0^1 \sqrt{\gamma'(s)^{\mathrm{T}} \boldsymbol{M}(s) \gamma'(s)}\, \mathrm{d}s \tag{1}$$

where $\gamma(s)$, $s \in [0, 1]$ is a parametric representation of the edge γ. In fact, Equation (1) defines a Riemannian metric, with the length of an edge γ being the measure of the interpolation

Copyright © 2002 John Wiley & Sons, Ltd.

error over that edge. Constructing a mesh with equal edges in this metric would therefore be equivalent to equi-distributing the interpolation error over all edges.

3. MOVING-NODE SCHEME

Once the error estimate is evaluated over all edges, a nearly optimal mesh is sought by, as much as possible, equi-distributing this error through a moving-node scheme. In this approach, the mesh is viewed as a network of springs whose stiffness constant represents the corresponding edge-based error estimate. The optimal position of the vertices may be computed as the solution of an energy minimization problem. This requires, for each vertex J, finding the new co-ordinates x_J such that

$$\min_{x_J} \sum_I P_I(x_J) = \min_{x_J} \sum_I (x_I - x_J)^2 k_{IJ} \tag{2}$$

where I denotes all the vertices sharing an edge with vertex J, $P_I(x_J)$ and k_{IJ} are the potential energy and stiffness constant, respectively, of all springs sharing the node J. These stiffness constants are defined as the scaled value of the associated edge in the Riemannian metric, that is

$$k_{IJ} = e(x_I - x_J)/||x_I - x_J|| \tag{3}$$

where $||x_I - x_J||$ is the Euclidean length of the edge between the vertex J and I, and $e(x_I - x_J)$ is the error estimate over this edge as defined by Equation (1).

Determining x_J that minimizes expression (2) is replaced by finding the root of the following equation:

$$\sum_I (x_I - x_J) k_{IJ} = 0 \tag{4}$$

which is the gradient of Equation (2) describing the equilibrium state of a spring network. It should be noticed that in general the metric $\boldsymbol{M}$ is not necessarily constant over an edge, so assuming that the spring stiffness k_{IJ} is constant is akin to a linearization.

Equation (4) is numerically solved with a fixed point method of the form $x^{n+1} = g(x^n)$ written as follows:

$$x_J^{n+1} = x_J^n + \omega \sum_I (x_I - x_J^n) k_{IJ}^n \tag{5}$$

where ω is a relaxation factor. Convergence of the method is achieved only for a spectral radius of the Jacobian matrix of $g(x^n)$ smaller than unity. Using Equation (5), the Jacobian matrix of $g(x^n)$ can be shown to be

$$[Dg(x_J^n)] = \begin{bmatrix} 1 - \omega \sum_I k_{IJ}^n & 0 \\ 0 & 1 - \omega \sum_I k_{IJ}^n \end{bmatrix} \tag{6}$$

with k_{IJ}^n approximated by constants. The spectral radius is then $|1 - \omega \sum_I k_{IJ}^n|$, and the convergence condition leads to $0 < \omega \sum_I k_{IJ}^n < 2$, where ω and the k_{IJ}^n's are all positive.

Copyright © 2002 John Wiley & Sons, Ltd.

This local scaling of the relaxation factor, $\tilde{\omega} = \omega(\sum_I k_{IJ}^n)$, can be replaced by a more suitable convergence condition, that is $0 < \tilde{\omega} < 2$. The fixed point method $x^{n+1} = g(x^n)$ may be then rewritten as

$$x_J^{n+1} = x_J^n + \tilde{\omega} \frac{\sum_I (x_I - x_J^n) k_{IJ}^n}{\sum_I k_{IJ}^n} \tag{7}$$

where the Jacobian matrix of $g(x^n)$ is $\mathrm{Diag}(1 - \tilde{\omega})$.

If $\tilde{\omega} = 1$, the Jacobian matrix of the fixed point method vanishes, the spectral radius also vanishes and fixed point method (7) converges in a single iteration. This case is nothing but a weighted baricenter, with the k_{IJ}^n's acting as weights. In the actual problem, which is non-linear, the k_{IJ}^n are not constant and it would thus take a few iterations to converge, but the linearization seems to be robust.

The convergence of the present fixed point method being proven, the robustness can be assured by explicitly imposing a set of user-specified constraints. The constraints can be that boundary nodes can only move along their respective curves, that the area of elements must remain positive, that quadrilateral elements must remain convex, that length of edges be bounded by minimum/maximum values, etc. If the initial grid satisfies these constraints, and if each node movement during adaptation is verified not to violate them, then the final adapted grid will also satisfy these constraints.

The adaptation procedure is coupled to the flow solver through an iterative loop. Finite Element Navier–Stokes Analysis Package in 2D (FENSAP2D) [6] is used as the flow solver for all test cases. It is based on a Galerkin-FEM, with a second-order artificial dissipation. Coupling to mesh adaptation is repeated until the lowest permitted value of the artificial dissipation is reached.

4. NUMERICAL RESULTS

4.1. Analytical (non-CFD) test cases

The moving-node scheme is first validated on two analytical test cases comprising structured triangular and quadrilateral grids. The idea is to demonstrate that a uniform metric will result in a uniform mesh in the Euclidean sense.

Using a mesh generator, a square/triangular computational domain is meshed as regularly as possible. Then, with a mesh editor, each node is moved to create a severely skewed mesh, without violating the topology. The metric is then set to a constant, i.e. mimicking a problem with constant second derivatives. This very particular situation results in a linear moving-node scheme, which is not generally the case. The moving-node scheme is applied with different values of $\tilde{\omega}$ in the interval $[0, 2]$ in order to study the effect of the relaxation factor on the convergence rate.

The adaptation for the two test cases, if optimal, ought to result in a structured quadrilateral grid for the square domain, as shown in Figure 1, and a structured triangular mesh for the triangular domain, as depicted in Figure 2. Each of these adapted meshes is accompanied by convergence plots that demonstrate the convergence of the moving-node scheme for values of $\tilde{\omega}$ in the interval $]0, 2[$.

Copyright © 2002 John Wiley & Sons, Ltd.

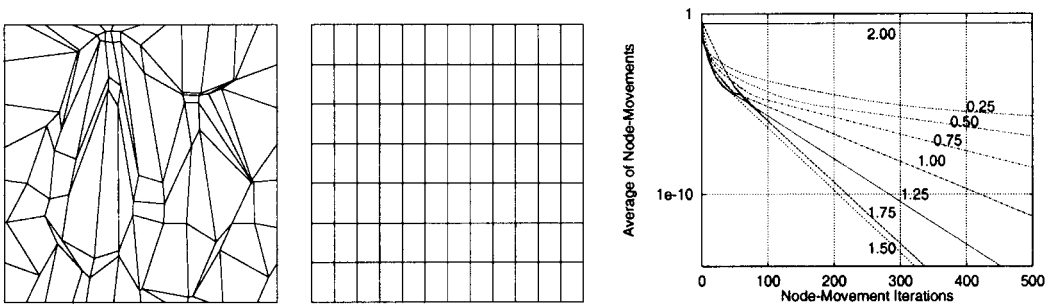

Figure 1. Quadrilateral grid case: initial grid (left), adapted grid (centre) and convergence of moving-node scheme for different values of $\tilde{\omega}$ (right).

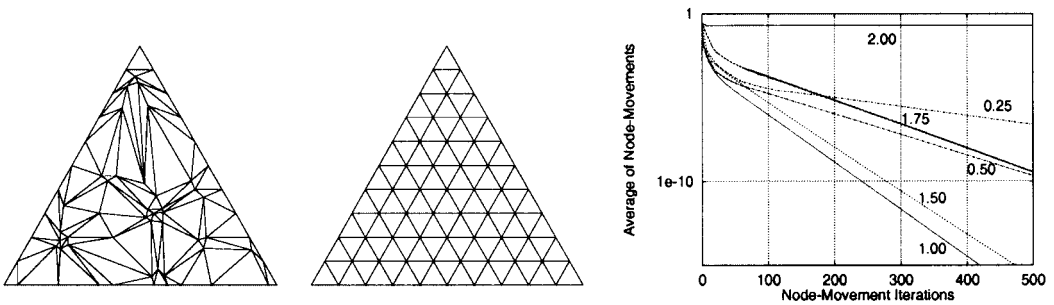

Figure 2. Triangular grid case: initial grid (left), adapted grid (centre) and convergence of moving-node scheme for different values of $\tilde{\omega}$ (right).

From those results, it can be clearly seen that the present methodology has no problem recovering uniform grids for a constant error target throughout the domain. However, the choice of relaxation factor may reduce the moving-node iterations by half. For instance, the highest convergence rate for the quadrilateral grid is reached with an over relaxation of 1.5, while $\tilde{\omega}=1$ required twice the number of iterations to reach the same accuracy. In the case of a triangular mesh, $\tilde{\omega}$ closer to unity gives the fastest convergence.

It should be pointed out that in practice, the adaptation procedure requires less iterations by cycle, since the node movement ought to be stopped at 10^{-6}. Experience shows that the method remains quite robust in the general non-linear case, but with lower relaxation factors and rates of convergence.

4.2. CFD test cases: coupling adaptation and solver

In these examples, the AGARD01–05 test cases of the AGARD Working Group 07 [4] are presented to validate the coupling of the present moving-node scheme with a flow solver. They consist of inviscid, transonic and supersonic external flows over a NACA 0012 airfoil. The free-stream conditions are summarized in Table I and the flow fields include shocks, either attached or detached, which are difficult to capture, particularly on coarse grids.

Figure 3 gives a general view and a zoom of the starting 200×40 C-grid, embedded in a 50-chord domain. This mesh is clearly not appropriate for simultaneously resolving all types

Copyright © 2002 John Wiley & Sons, Ltd.

Table I. Free-stream Mach number (M^a_∞) an angle of attack (AoA) for the AGARD01–05 test cases.

Test cases	M^a_∞	AoA
AGARD01	0.80	1.25°
AGARD02	0.85	1.00°
AGARD03	0.95	0.00°
AGARD04	1.20	0.00°
AGARD05	1.20	7.00°

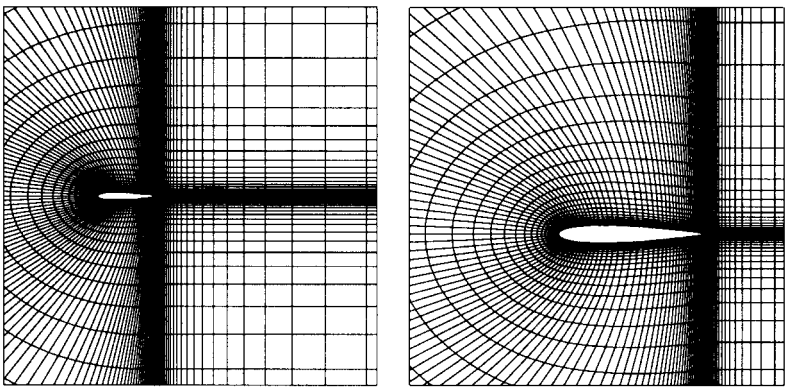

Figure 3. Initial 200×40 C-grid over a NACA 0012: general view (left) and zoom of airfoil region (right).

of shocks (bow, normal, strong, weak, oblique, fishtail) occurring in the five test cases due to the range of Mach numbers. It will, however, be shown that it can serve as an initial grid for mesh adaptation, for all Mach numbers. To push the equi-distribution of the error as far as possible, 30–40 adaptation–solution couplings are performed in all test cases, with, at each adaptation step, several hundred moving-node loops. In practice, however, five adaptation–solution couplings are amply sufficient to capture most of the relevant physical phenomena.

Figures 4–8 show the final adapted grids and the pressure and Mach contours of the corresponding solutions. These C-grids, while highly skewed, respect the topology of the starting grid, except for nodal location. They permit, however, a much sharper prediction of shocks, clearly demonstrating that grid skewness can only be judged in the context of the local phenomenon that the grid is used to resolve.

Figure 6 displays the results for the AGARD03 test case. This transonic flow at $Ma = 0.95$ and $\mathrm{AoA} = 0°$ is characterized by a fishtail shock: two oblique shocks emanating from the trailing edge which intersect a weak normal shock in the wake. The normal shock is relatively weak with a Mach number smaller than 1.1. Numerical investigations have indicated that the location of the downstream normal shock is quite sensitive to grid and that reliable results can only be obtained using a very fine grid or an adapted one.

The results for a supersonic flow at $Ma = 1.2$ and $\mathrm{AoA} = 0°$ and 7° are shown in Figures 7 and 8, respectively. Such flows are characterized by a detached bow shock and an oblique

Copyright © 2002 John Wiley & Sons, Ltd.

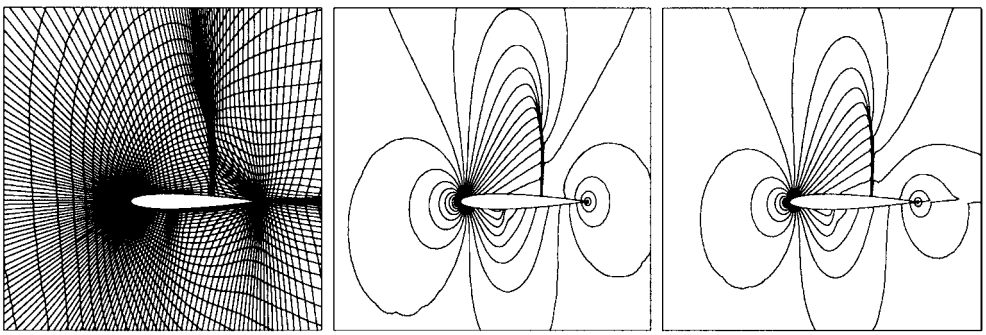

Figure 4. AGARD01 test case: final adapted grid (left), pressure contours (centre) and Mach contours (right).

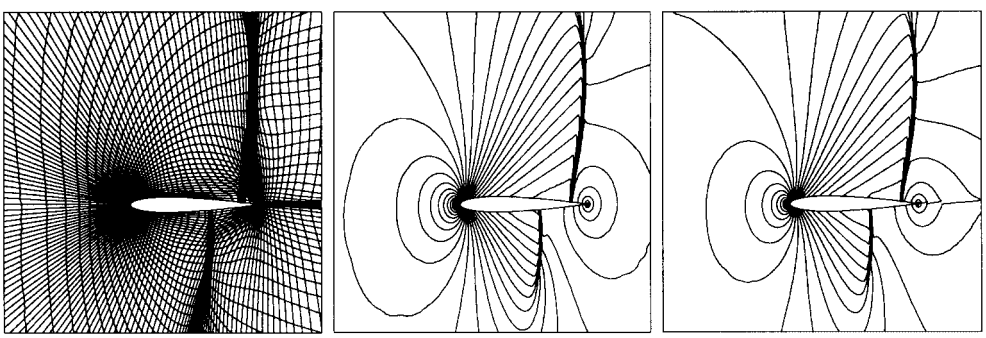

Figure 5. AGARD02 test case: final adapted grid (left), pressure contours (centre) and Mach contours (right).

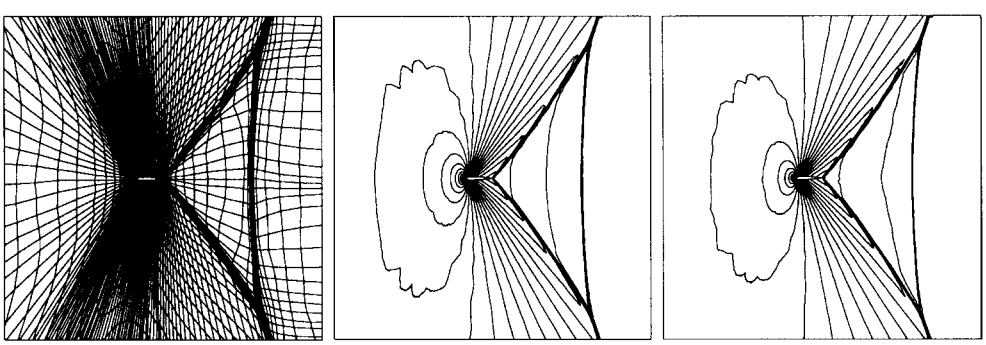

Figure 6. AGARD03 test case: final adapted grid (left), pressure contours (centre) and Mach contours (right).

Copyright © 2002 John Wiley & Sons, Ltd.

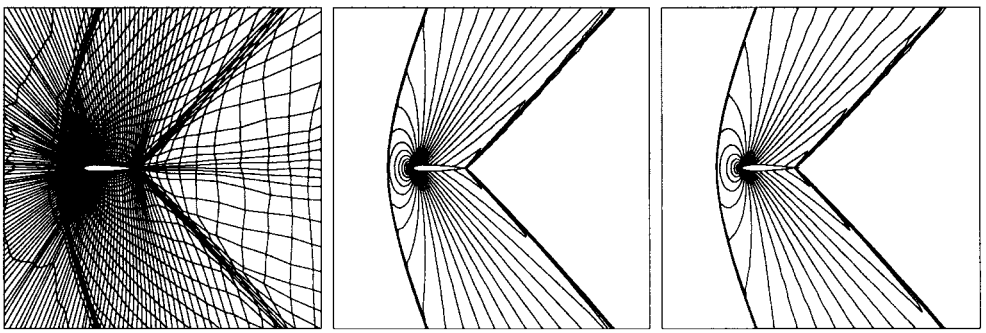

Figure 7. AGARD04 test case: final adapted grid (left), pressure contours (centre) and Mach contours (right).

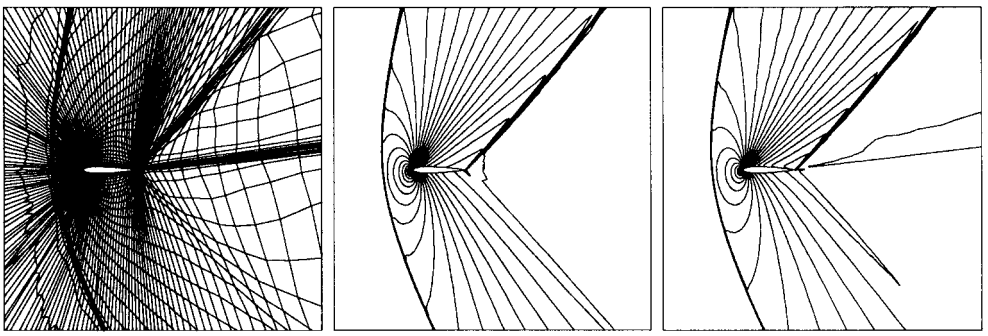

Figure 8. AGARD05 test case: final adapted grid (left), pressure contours (centre) and Mach contours (right).

shock structure emanating from the trailing edge. It is not an exaggeration to say that it is difficult to find many CFD solvers capable of computing, on the initial grid displayed in Figure 3, sharp and accurate solutions like those shown in Figures 7 and 8. This confirms that grid adaptation is a very efficient way to capture shocks.

The wall pressure coefficient distributions (C_p) of the AGARD01–05 test cases are compared against Pulliam and Barton (P&B) adapted results [7] which were computed on a 560×65 C-grid and a 48-chord domain. This is approximately 4.5 times more nodes than the grid used in the current calculations. In addition, P&B [7] adapted their grid by *manually* clustering nodes in regions with abrupt variations. It is obvious that these regions had to be *a priori* identified by solving on coarser grids. Thus P&B's hindsight approach is not as general as the present *a posteriori* approach, which is entirely automatic, with no user intervention in the solution process. Any other alternative would be rather difficult to generalize to bow or fishtail shocks.

Figure 9 illustrates C_p comparisons for the AGARD01 (left) and the AGARD02 (right) test cases, respectively. Overall, these figures show good agreement, with the results of P&B slightly better in capturing the pressure surface's weak shock for the AGARD01 test case.

Copyright © 2002 John Wiley & Sons, Ltd.

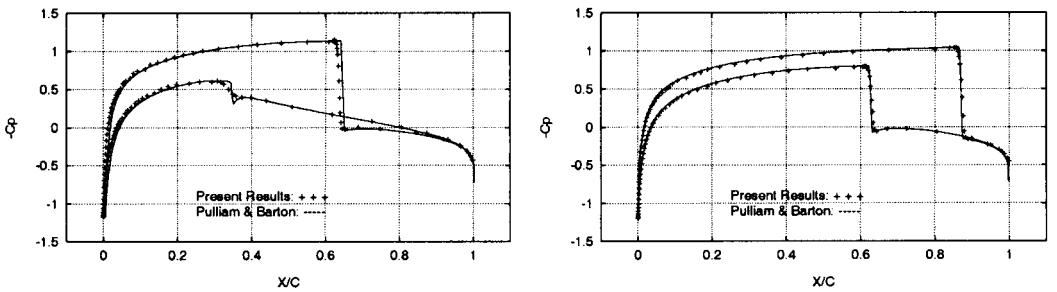

Figure 9. Comparison of pressure coefficient with Pulliam and Barton [7]: AGARD01 (left) and AGARD02 (right).

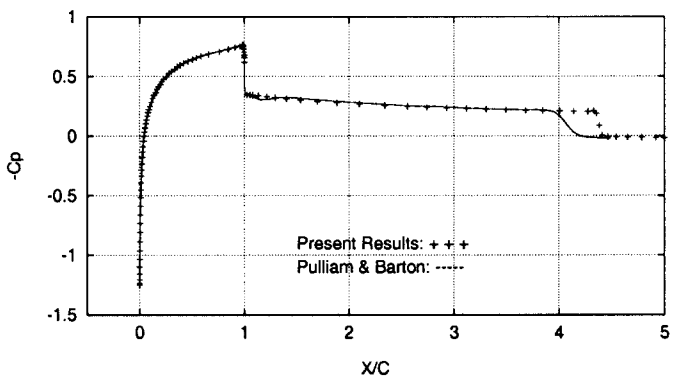

Figure 10. Comparison of pressure coefficient with Pulliam and Barton [7] for the AGARD03 test case.

Figure 10 compares, for the AGARD03 test case, the pressure coefficient on the airfoil and behind the trailing edge on a horizontal cut. Again, there is good agreement between the present predictions and the results of Reference [7]. The weak shock is, however, predicted at different locations and with different slopes. It is clear that the shocks computed on the adapted grid are slightly better than those of P&B.

The position of the weak shock is at 3.1 chords behind the trailing edge for the P&B solution, against 3.37 chords on the current adapted grid. A grid dependency study performed by Warren *et al.* [8] on $65 \times 25, 129 \times 49, 257 \times 97$ and 2049×765 C-grids, in a 100-chord domain, has shown that the weak shock asymptotically moves to a location 3.35 chords behind the trailing edge on their finest mesh, which was approximately 200 times finer than the present grid. Their conclusion is that with even further extrapolation, the position of the weak shock, on an asymptotically infinitely fine grid, would be 3.32 chords behind the trailing edge; very close to the mesh adaptation prediction.

Figure 11 compares pressure coefficient distributions with Reference [7] for the AGARD04 (left) and AGARD05 (right) test cases. It reveals good agreement between the adapted solution and P&B results, obtained using much finer grids. The proposed methodology, however, permits an even better resolution of the detached as well as trailing edge shocks.

Copyright © 2002 John Wiley & Sons, Ltd.

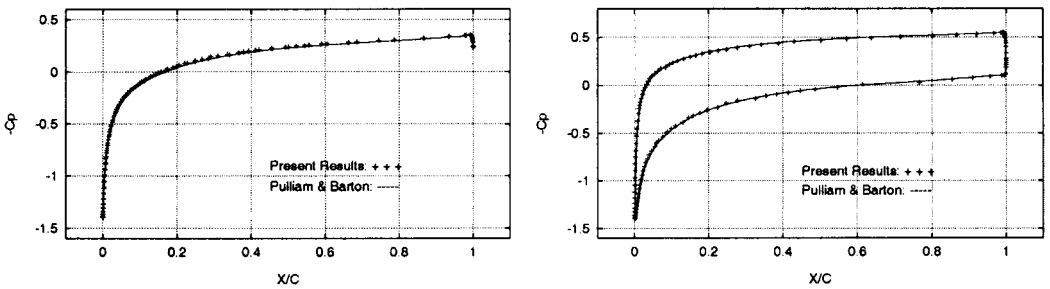

Figure 11. Comparison of pressure coefficient with Pulliam and Barton [7]: AGARD04 (left) and AGARD05 (right).

Table II. Comparison of lift and drag coefficients with Pulliam and Barton [7] for AGARD01–05 test cases.

Test case	Pulliam and Barton		FENSAP2D		% Difference	
	Lift	Drag	Lift	Drag	Lift	Drag
AGARD01	0.3618	0.0236	0.3541	0.0231	2.1	2.1
AGARD02	0.3938	0.0604	0.3872	0.0598	1.7	1.0
AGARD03	0.0000	0.1103	0.0001	0.1092	0.0	1.0
AGARD04	0.0000	0.0968	0.0004	0.0954	0.0	1.4
AGARD05	0.5232	0.1554	0.5237	0.1544	0.1	0.6

Table III. Statistical data for the error estimate distributions over the initial and adapted grids.

Test case	Initial grid			Adapted grid		
	$E_{\min}$	$E_{\max}$	σ^2	$E_{\min}$	$E_{\max}$	σ^2
AGARD01	0.00026	5.9	0.81	0.0086	9.2	0.43
AGARD02	0.00024	5.5	0.81	0.0117	14.1	0.44
AGARD03	0.00043	6.2	0.80	0.0233	8.7	0.47
AGARD04	0.00024	7.5	1.35	0.0061	10.6	0.34
AGARD05	0.00022	7.4	1.41	0.0110	9.7	0.39

To wrap up the comparison, lift and drag coefficients are presented in Table II. Overall, the results are in good agreement, thus validating the flow solver, the grid adaptation procedure and their coupling strategy. Furthermore, it is demonstrated that accurate predictions require less preparation time and computer effort if adapted meshes are used.

To study how well the adapted grid fits the flow features, a statistical analysis is performed on the error estimate distribution. These characteristics are summarized in Table III for the AGARD01–05 test cases. The columns $E_{\min}$, $E_{\max}$ and σ^2 represent the minimum error level, the maximum error level and the variance of the error distribution, respectively. The grid data is normalized in such a way that the average is equal to unity. Essentially, one may observe that the variance parameter is reduced by a factor of 2.5 on the average for all adapted grids, proving a better equidistribution of the error.

Copyright © 2002 John Wiley & Sons, Ltd.

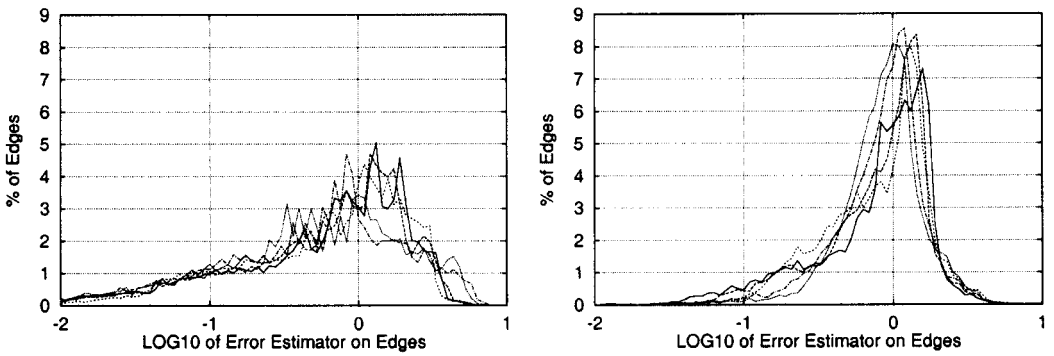

Figure 12. AGARD01–05 test cases: error distributions on the initial grid (left) and adapted grids (right).

Another alternative to analyse the error distribution is through a histogram plot. Figure 12 shows the number of edges in percentage as a function of the non-dimensional error levels for all the test cases. Ideally, all the edges of an adapted grid should have the same error. In practice, a nearly Gaussian distribution is obtained, where the minimum error (i.e. the spreading of the error) is reduced by an order of magnitude. Note also that for all the test cases, the final adapted grids are statistically more suited than the initial grid to resolve all the flow field with nearly the same accuracy.

5. LIMITATIONS OF ADAPTED STRUCTURED GRIDS

After presenting the moving-node scheme and its validation on generic and CFD benchmarks, a study of some pathological cases, due to constraints inherent to structured grids, is presented.

5.1. Impossibility of structured grid alignment

An anisotropic grid adaptation moves the nodes such that the element edges are aligned with directional features of the solution. When in some cases this is impossible, the method is no longer optimal. For example, a 200×40 O-grid is composed of 200 radial curves that extend from the wing to the outer boundary, and 40 circular curves that turn around the wing. As the moving-node scheme aligns nodes with directional features of the solution, the circular curves family will be aligned with the detached bow shock in front of the leading edge and the radial curves will cross it without being really affected (see Figure 13 on left).

At the opposite end, near the far field, the detached bow shock is more or less radiant to the domain. In this case, the family of radial lines is the one which is aligned with the shock (see Figure 13 on right). Somewhere in the computational domain, the detached bow shock must switch from the circular curves family to the radial curves family along a transition region that is characterized by misalignment of the mesh with the solution feature. This leads to the appearance of a rhombus in the grid and oscillations and/or dissipation in the solution.

Copyright © 2002 John Wiley & Sons, Ltd.

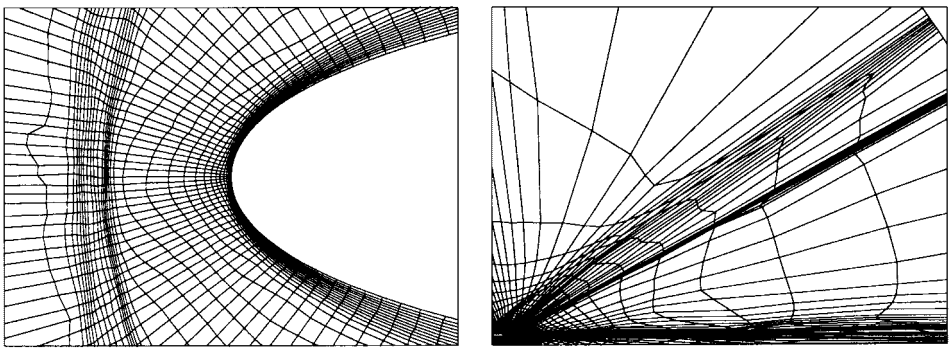

Figure 13. Final adapted O-grid over a NACA 0012 for flow conditions of $Ma = 2$, $Re = 10\,000$ and $\mathrm{AoA} = 0°$. Left: zoom on the leading edge. Right: region of the bow shock from the leading edge to the far field.

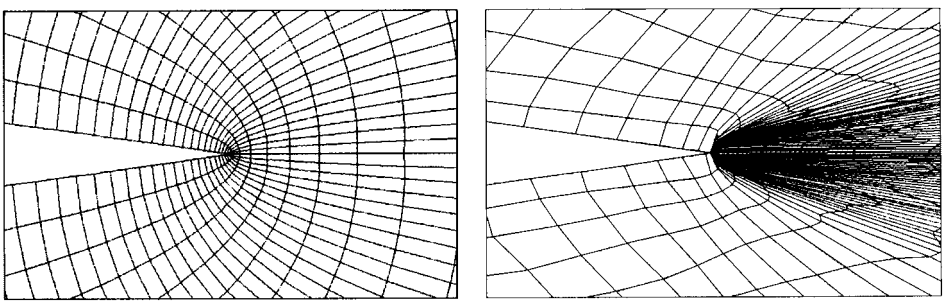

Figure 14. Zoom of the NACA 0012 O-grid in the trailing edge region: initial grid (left) and adapted grid (right).

5.2. Possible low resolution of geometric singularities

A boundary node of an O-grid, is usually surrounded by two quadrilateral elements, and the adjacent computational domain is approximately a half-plane (see Figure 14 on left). A problem occurs if the boundary is not smooth, in particular, at singular points like the trailing edge vertex where the boundary acts more as a full-plane than a half-plane, resulting in two skewed quadrilateral elements. In fact, as displayed in Figure 14 (right), the node-moving scheme clusters quadrangles at the trailing edge.

This problem can be avoided by using a C-grid around the airfoil. One characteristic of a C-grid is that there is a boundary node which belongs to four elements. Usually, it is convenient to put this singular node on the trailing edge such that the singularity of the mesh fits the singularity of the domain. The mesh in the vicinity of the trailing edge is approximately orthogonal and the adapted grid is much better (see Figure 15). Thus the behaviour is function of the grid structure choice.

A standard way to deal with complex geometries with many corners is to divide the structure. It can be a *h*-method with hanging nodes or simply a pure unstructured mesh. Another alternative is to use structured multi-blocks to fit complex geometries and corners. This task is

Copyright © 2002 John Wiley & Sons, Ltd.

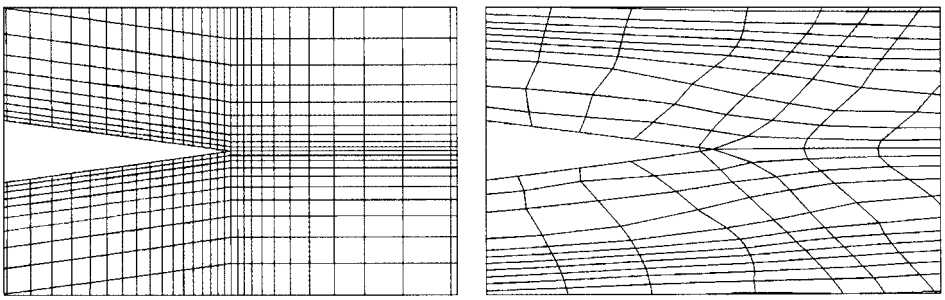

Figure 15. Zoom of the NACA 0012 C-grid in the trailing edge region: initial grid (left) and adapted grid (right).

generally not automatic, is labour intensive, time consuming and often requires trial and error when, as the computation proceeds, the initial blocking may reveal itself not to be entirely appropriate. Despite such inconveniences, it remains an effective way to deal with complex geometries.

5.3. The equidistribution of the error estimate is limited

A 2-D structured grid may be viewed as the product of two families of 1-D grids: vertical and horizontal 1-D grids. Applying a spring analogy procedure does not equidistribute the error over all edges of the grid, but rather causes an error equidistribution within each family of 1-D grids. In other words, the edge-based error estimate will be approximately uniform within each family of 1-D grids, but different from the other family of 1-D grids.

To illustrate this problem, let us consider a square domain with $M \times N$ grid points and a constant error metric, as already shown in Section 4.1. Applying the spring analogy of Section 3 produces a uniform grid for both cases: $M = N$ and $M \neq N$. If $M = N$ the adapted grid will be formed of perfectly square elements and the error will be equidistributed over all edges. In the second case, where $M \neq N$, the adapted elements will have a rectangular shape but the family of vertical 1-D grids will have a different error estimate than the family of horizontal 1-D grids. This is to be expected since in the case of a constant metric, the adapted mesh is optimal in the common Euclidean sense and therefore the error estimate cannot be equidistributed over all edges in the case $M \neq N$.

This drawback can also be shown through a CFD problem of a viscous flow at $Ma = 0.85$, $Re = 5000$ and $\mathrm{AoA} = 0^\circ$ over a NACA 0012 airfoil. The computational domain consists of a 50-chord radius circle and 200×40 O-grid points. Figure 16 (left) shows that the clustering of nodes in the boundary layer, shock and wake, results in a more appropriate grid than the initial one, for resolving the previous listed flow features. However, this adapted grid is far from being optimal or suitable as the adapted unstructured triangular mesh with 9512 nodes displayed in Figure 16 (right). It is obvious that in the case of a quadrilateral element grid, the inherent structure restricts the equidistribution of the error and the use of only 40 nodes in the wake region is a sure way to miss the von Karman vortex street.

Copyright © 2002 John Wiley & Sons, Ltd.

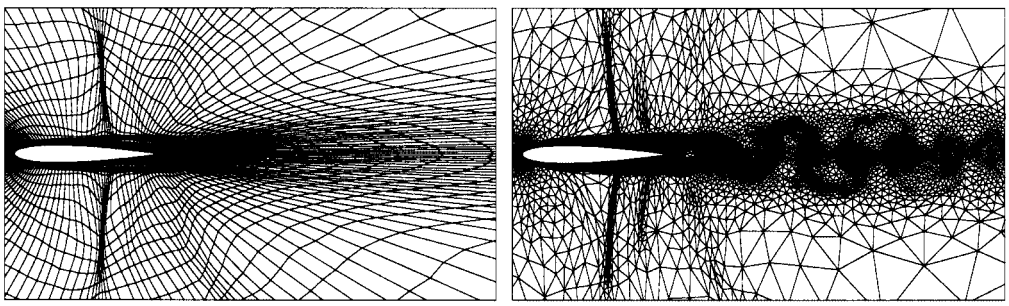

Figure 16. Flow at $Ma = 0.85$, $Re = 5000$ and $\mathrm{AoA} = 0^\circ$: structured adapted mesh (left) and unstructured adapted mesh (right).

6. UNSTRUCTURED MESHES

Details of the anisotropic adaptation of unstructured meshes and its validation will be presented in Part III of this paper series. As a precursor, however, the current section compares the moving-node scheme on structured grids to *h–r* adapted unstructured meshes for the same AGARD01–05 test cases. The objective is to vividly demonstrate, through unstructured grids, that 'different flow conditions' call for 'drastically different grids', even if the geometry remains unchanged. Furthermore, iteration is carried out much farther with the more flexible unstructured grid topology, to achieve the best possible equi-distribution of error.

For each test case:

- the adapted (final) structured grid and its respective solution (Figures 4–8) is used as background grid and (frozen) solution for the unstructured-mesh-optimization process,
- the initial triangular mesh is created by dividing each element of the corresponding adapted quadrilateral grid into two triangles,
- no further flow solver is used and the error estimate is computed directly from the frozen final structured solution,
- all mesh-optimization parameters are set to the same values as those used to adapt the corresponding structured grid.

Thus, any improvement in the solution can be seen as the 'pure bonus' that would result from converting a structured grid into an unstructured one.

Figures 17 and 18 show the adapted unstructured meshes for the AGARD01–05 test cases. One may observe that the clustering of nodes is taking place in the same regions as in the corresponding adapted structured grids. This is to be expected since both structured and unstructured meshes were adapted from the same solutions. However, with unstructured mesh adaptation, there are no more problems with grid alignment, constant connectivity, management of geometric singularities and complex geometries with special blocking and so on.

Table IV gives some statistics on node and error distributions of adapted unstructured meshes for the AGARD01–05 test cases. The columns are N_{N}, total number of nodes, N_{C}, number of elements, N_{E}, number of edges, N_{w}, number of nodes on the wall, N_{∞}, number of nodes at the outer boundary, $E_{\min}$, minimum error level, $E_{\max}$, maximum error level and σ^2 is the variance of the error distribution. Here again, the grid data is normalized in such a way that the average is equal to unity.

Copyright © 2002 John Wiley & Sons, Ltd.

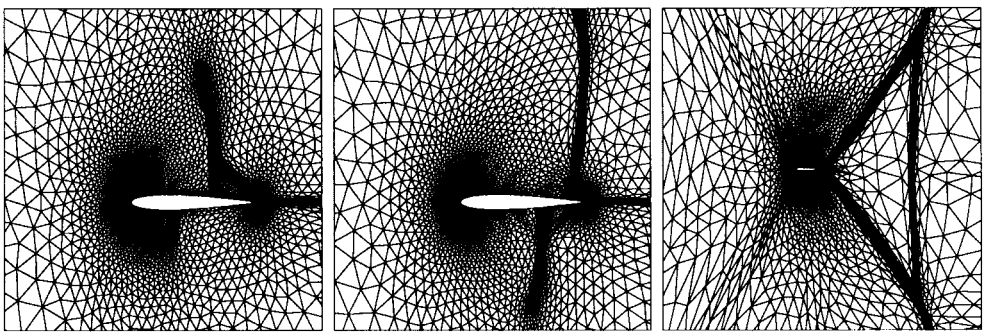

Figure 17. Adapted unstructured meshes: AGARD01 (left), AGARD02 (centre) and AGARD03 (right).

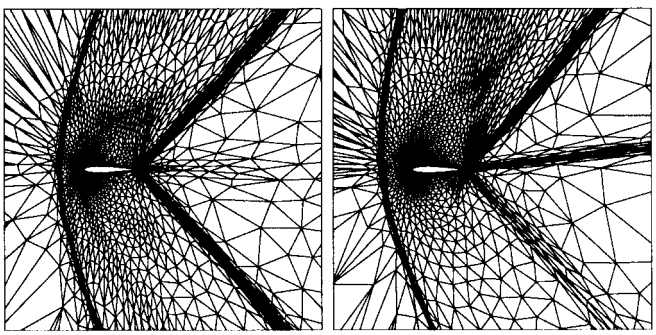

Figure 18. Adapted unstructured meshes: AGARD04 (left) and AGARD05 (right).

Table IV. Statistical data on node and error distributions of adapted unstructured meshes for AGARD01–05 test cases.

Test cases	N_N	N_C	N_E	N_w	N_∞	E_{min}	E_{max}	σ^2
AGARD01	8184	16 032	24 216	267	69	0.51	1.43	0.0068
AGARD02	8161	16 006	24 167	244	72	0.55	1.40	0.0067
AGARD03	8199	16 169	24 368	141	88	0.49	1.50	0.0072
AGARD04	8332	16 421	24 753	119	124	0.47	2.19	0.0092
AGARD05	8120	15 946	24 066	126	168	0.53	1.57	0.0093

Recalling that the initial C-grid is composed of 8000 quadrangles, 16 205 edges and 8205 nodes with 130 nodes on the wing and 280 nodes on the outer boundary. Table IV shows that when the error estimate is equi-distributed, 130 nodes on the wing are not enough for the AGARD01–03 cases and 280 nodes on the outer boundary is excessive for all considered configurations. Comparing the variance of the error estimate, given by the last column of Table IV, against that of the initial grid, displayed in the fourth column of Table III for structured grids, shows a 53-fold reduction, while this ratio is limited to 2.5 in the case of structured grids. This becomes even more evident when examining Figure 19, which represents a comparison of error distributions before and after adaptation, for structured (ten curves of the

Copyright © 2002 John Wiley & Sons, Ltd.

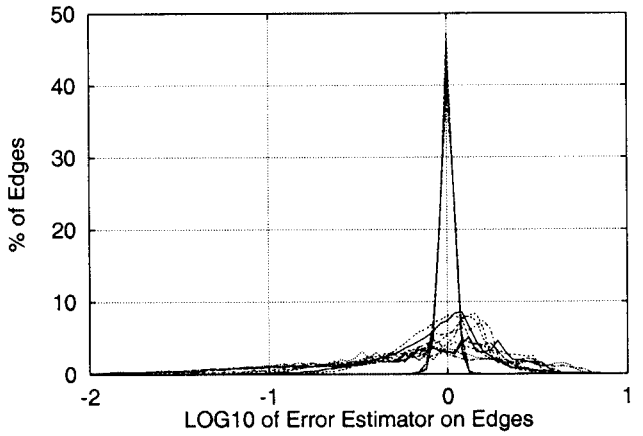

Figure 19. AGARD01–05 test cases: error distribution on the initial and adapted structured grids (Figure 12 is reported here), and on adapted unstructured meshes (five narrower Gaussian).

two plots of Figure 12) and unstructured (five narrower curves) grids for all the AGARD test cases. It shows that in the case of structured grids, the moving-node scheme greatly reduces the error spread, with a more-or-less Gaussian distribution and a narrower variance. The five much narrower Gaussian distributions (imperceptible from one another) clearly demonstrate how more flexible unstructured meshes are in producing a completely uniform error estimate (within a specified bound). Keeping a constant connectivity table for structured grids reduces the potential for equi-distributing the error and also limits anisotropy.

7. CONCLUSION

A directional (anisotropic, as opposed to just mesh refinement) grid adaptation method, based on an *a posteriori* edge-based error estimate, has been described for quadrilateral grids and applied to a wide range of external compressible flows. The error estimator is measured by taking the second derivatives of the numerical solution and the resulting Hessian tensor is used to define a Riemannian metric. An improved node movement scheme with no orthogonality constraint is introduced to as much as possible equalize the length of element edges in the defined metric. The adaptive procedure is validated on analytical test cases, as well as on transonic and supersonic benchmarks. It has been proven to be effective for a wide range of flow conditions.

This mesh optimization technique does not use any refinement/coarsening operations that may lead to hanging nodes. Therefore it can be easily incorporated with any existing structured flow solver without any major changes. It has been proven to be robust and converge well for a wide variety of test cases. It is considered a cost-effective way to increase accuracy.

Nothing being perfect, however, there are limitations to the method for structured grids, the major one being the constant connectivity of the grid (in order to keep the method portable) which limits the level of equi-distribution of the error. Nevertheless, it is believed that the moving-node scheme introduced in this paper is in some sense the best possible one. But to

Copyright © 2002 John Wiley & Sons, Ltd.

unlock the full power of any mesh optimization, the use of unstructured meshes should be considered. This will be the focus of the next article of the three-part paper series [9] and will show how user: initial mesh and flow solver-independence can be achieved.

REFERENCES

1. Löhner R, Morgan K, Zienkiewicz OC. Adaptive grid refinement for the compressible Euler equation. In *Accuracy Estimates and Adaptive Refinements in Finite Element Computation*, Babuška I, Zienkiewicz OC, Gago J, Oliveira A (eds). Wiley: New York, 1986.
2. Peraire J, Vahdati M, Morgan K, Zienkiewicz OC. Adaptive remeshing for compressible flow computations. *Journal of Computational Physics* 1987; **72**:449–466.
3. Oden JT, Strouboulis T, Devloo P. Adaptive finite element methods for high-speed compressible flows. *International Journal for Numerical Methods in Fluids* 1987; **7**:1211–1228.
4. Jones DJ. Test cases for inviscid flow field methods: reference test cases and contributions. *Technical Report AR*-211, AGARD, NATO, 1985.
5. Habashi WG, Fortin M, Vallet M-G, Dompierre J, Bourgault Y, Ait-Ali-Yahia D, Tam A. Anisotropic mesh adaptation: towards user-independent, mesh-independent and solver-independent CFD solutions. Part I: Theory. *International Journal for Numerical Methods in Fluids* 2000; **32**:725–744.
6. Baruzzi GS, Habashi WG, Guevremont G, Hafez MM. A second order finite element method for the solution of the transonic Euler and Navier–Stokes equations. *International Journal for Numerical Methods in Fluids* 1995; **20**:671–693.
7. Pulliam TH, Barton JT. Euler computation of AGARD working group 07 airfoil test cases. In *AIAA 23rd Aerospace Sciences Meeting*, AIAA-85-0018, January 1985.
8. Warren GP, Anderson WK, Thomas JL, Krist SL. Grid convergence for adaptive methods. In *AIAA 29nd Aerospace Sciences Meeting*, AIAA-91-1592-CP, January 1991.
9. Dompierre J, Vallet M-G, Bourgault Y, Fortin M, Habashi WG. Anisotropic mesh adaptation: towards user-independent, mesh-independent and solver-independent CFD solutions. Part III: Unstructured grids. *International Journal for Numerical Methods in Fluids* 2002; **39**:675–702.

Copyright © 2002 John Wiley & Sons, Ltd.